Carbon 186 (2022) 253–261

Contents lists available at ScienceDirect

Carbon

journal homepage: www.elsevier.com/locate/carbon

Research Paper

Q-carbon as a new radiation-resistant material

J. Narayan [a, *], P. Joshi [a], J. Smith [a], W. Gao [a], W.J. Weber [b], R.J. Narayan [c]

[a] Department of Materials Science and Engineering, North Carolina State University, Raleigh, NC, 27695-7907, USA
[b] Department of Materials Science and Engineering, University of Tennessee, Knoxville, TN, 37996-2100, USA
[c] Joint Department of Biomedical Engineering, North Carolina State University and UNC Chapel Hill, Raleigh, NC, 27695-7907, USA

ARTICLE INFO

Article history:
Received 12 August 2021
Received in revised form
12 September 2021
Accepted 2 October 2021
Available online 12 October 2021

Keywords:
Q-carbon
Radiation-resistant materials
Ion radiation damage

ABSTRACT

We have discovered that Q-carbon is extremely resistant to radiation damage under ion irradiations involving extreme atomic displacements and electronic excitations. Using 5 MeV Au^+ ions, the Q-carbon films on sapphire substrates were irradiated in the dose range 3.3–10 dpa (displacements-per-atom). After the ion irradiations, detailed studies on the atomic structure and bonding characteristics showed that atomic structure and bonding characteristics of amorphous Q-carbon remained essentially unchanged to 10 dpa of radiation damage, which is equivalent to over twenty years of neutron damage in a conventional reactor. There was an ion-beam mixed layer below the Q-carbon layer, whose thickness increased from 5 nm to 10 nm, as the dose increased from 3.3 to 10 dpa. This layer was found to be mostly amorphous with a mixture Al_2O_3 and Al_4C_3. This layer, formed as a result of enhanced forward scattering and ballistic ion beam mixing, exhibited composition consistent with detailed TRIM calculations. We also found that nanodiamonds (3 nm average size) embedded in Q-carbon grew to about 60 nm after 6.6 dpa and shrank to about 40 nm after 10 dpa. We discuss the mechanism for the growth and shrinkage of metastable phase of diamond under nonequilibrium ion irradiations.

1. Introduction

Integrity and variation in properties of materials under intense radiation is of critical importance for many applications ranging from nuclear power reactors to protective coatings for solid state devices [1–3]. Graphite and diamond related materials usually have poor radiation resistance, where graphite accumulates radiation damage in the form of vacancies and interstitials and their clusters, and diamond turns amorphous above a certain damage threshold energy. The displacement threshold energy, defined as energy to displace an atom and create a Frenkel pair, for graphite and diamond are reported to be 25 eV [4] and 45 eV [5], respectively. It is well established that energetic particles lose their energy via collisions with atoms (known as nuclear stopping) and interactions with electrons (electronic stopping). The nuclear stopping mostly creates displacement damage through elastic scattering with some component of inelastic scattering, whereas electronic stopping results in electronic excitations and energy transfer to phonons. Typical electron-phonon relaxation times are of order of picoseconds, so this rapid energy transfer to phonons may lead to local transient thermal spikes depending upon the spatial energy distribution [2,6,7].

The heavy ion irradiations provide an intense source of nuclear displacements and electronic excitations, which can be controlled by incident ion and substrate variables to cover almost all forms of radiation damage. The displacement damage in the form of Frenkel pairs (N_{FP}, vacancy-interstitial) can be estimated by calculating the damage energy (E_D) and using the formula ($N_{FP} = \alpha E_D/2E_d$), where E_d is the displacement threshold energy, which is a materials parameter, characteristic of bonding, and α (≈ 0.8) is the average constant taking into the recoil spectrum [3,6]. Using this framework, it was established that there is a critical damage energy (E_D*) at which there is a first-order phase transformation from crystalline to amorphous phase. By ion implantation and modeling the critical energies for Si and diamond were determined to be 12 eV/atom [3,6] and 16eV/atom [8], respectively. In the case of metals, most of interstitials and vacancies go their separate ways, where interstitials cluster as larger dislocation loops and vacancies as smaller dislocation loops and voids. With continued irradiation at higher temperatures, interstitials develop into forest of dislocations and vacancies into voids, causing swelling and materials failure eventually [1]. To overcome this problem, there has been a continuous effort to create radiation-resistant materials, where production of vacancies and

* Corresponding author.
E-mail address: narayan@ncsu.edu (J. Narayan).

https://doi.org/10.1016/j.carbon.2021.10.006
0008-6223/

interstitials is minimized, and residual defects are annihilated either through recombination or other modes of elimination. In the case of amorphous materials, vacancies create dangling bonds and interstitials lose their identity by attaching to nearby dangling bond in a random crystal structure [6,7].

To design a radiation-resistant material, we have reduced the defect production by increasing the damage threshold energy via choosing strongly bonded covalent materials, and promoted recombination and elimination of residual defects through random crystal structure. Using these considerations, we have created a new phase of carbon, named Q-carbon, where carbon is melted in a highly undercooled state by nanosecond laser pulses and quenched to form a random structure of diamond tetrahedra which has 50% higher density than the record number density in diamond of $1.77 \times 10^{23} cm^{-3}$ [9–14]. The bonding within the tetrahedra is sp^3 and in between sp^2 with overall sp^3 fraction exceeding over 80%. This unique structure has shown to be very stable thermally with record hardness of 60% higher than that of diamond [11]. Remarkably B-doped carbon shows a record BCS superconducting transition temperature of 57K and higher with increased boron concentration. This is quite consistent as hardness and BCS superconductivity are interlinked through Debye temperature and electron-phonon interaction [10,12,14].

2. Materials and methods

Amorphous carbon films about 500 nm thick were deposited on c-sapphire (0001) substrates (supplied by University Wafer Co.) using our pulsed laser deposition (PLD) system equipped with KrF laser. The operating pressure of the vacuum chamber was 1.0×10^{-6} to 5.0×10^{-7} Torr. Nanosecond laser pulses of a KrF excimer laser ($\lambda = 248$ nm, $\tau = 25$ ns) were used to ablate an amorphous carbon target mounted in the PLD chamber. The repetition rate and the laser energy density of the nanosecond laser were 10 Hz and 3.0–3.5 Jcm^{-2}, respectively. The ratio of sp^2 to sp^3 bonded carbon of the as-deposited amorphous carbon thin films was controlled by laser and substrate variables, including substrate temperature and pulse energy density and laser plume characteristics. Following the PLD process, amorphous carbon films were laser annealed by using nanosecond ArF excimer laser ($\lambda = 193$ nm, $\tau = 20$ ns). The laser energy density used during the pulsed laser annealing (PLA) ranged from 0.6 to 1.2 Jcm^{-2}. The PLA melts the amorphous carbon (a-carbon) into a highly undercooled state of molten carbon and subsequently quenches the undercooled state to form graphene, α-carbon, diamond or Q-carbon (with increasing undercooling) [14]. Q-carbon was formed when a laser energy density ranging from 0.6 to 0.7 Jcm^{-2} was used. It should also be noted that the degree of undercooling was dependent on the laser parameters and thermal conductivities of the substrate and as-deposited films. Therefore, the laser parameters for the formation of Q-carbon and diamond were different for different substrates.

After PLA the c-sapphire samples contained 100 nm Q-carbon layer followed by 400 nm thick α-carbon. Three multi-layered samples (~1 cm × 1 cm) containing the 100 nm thick Q-carbon layer were irradiated with 5 MeV Au ions at 300 K using the 3 MV tandem accelerator in Ion Beam Materials Laboratory (IBML) at the University of Tennessee [15] to fluences of 2.9, 5.9 and 8.8×10^{15} ions/cm^2, respectively. The ion beam was rastered at scanning frequencies of 517 and 64 Hz for the horizontal and vertical directions, respectively, over an irradiated area of 0.5 cm × 1 cm, to ensure a uniform irradiation over the irradiated area, which left half of each sample unirradiated for comparison. The average ion flux over the irradiated area was 1.9×10^{12} ions/cm^2s, with corresponding irradiation times of 0.42, 0.86 and 1.29 h, respectively. Sample heating from energy transfer to phonons was estimated to be less than 10 K for these irradiation conditions. The irradiations were performed under a vacuum below 2.0×10^{-7} Torr. The depth profiles of damage production, incident ion concentration, electronic and nuclear energy loss, and atomic mixing were calculated using the Stopping and Range ion Ions in Matter (SRIM) code [16] in full-cascade mode as recently recommended [17]. In the SRIM calculations, densities of 1.8, 5.0 and 3.98 g/cm^3 were assumed for α-carbon, Q-carbon and sapphire (Al_2O_3), respectively, and displacement energies of 28, 25 and 28 eV were assumed for C, Al and O, respectively.

The characterization of the Q-carbon and diamonds were performed using high-resolution scanning electron microscopy (HRSEM), (scanning) transmission electron microscopy (STEM and TEM), core-loss EELS, electron dispersive X-ray spectroscopy (EDS), Raman spectroscopy, and electron backscatter diffraction (EBSD). The HRSEM was performed using secondary and back-scattered electrons (having a sub-nanometer resolution) by using FEI Verios 460L SEM. The aberration-corrected STEM-FEI Titan 80–300, JEOL 2000 FX, 2010F, and FEI Talos F200X were used to perform the (scanning) transmission electron microscopy. The EELS scans were performed by using the EELS detector mounted in the STEM-FEI Titan 80–300 microscope. The Raman measurements were made using the Alfa300 R superior confocal Raman spectroscope (lateral resolution <200 nm) having 532 nm excitation source. The Raman spectrometer was calibrated by using a standard crystalline Si sample with a vibrational mode (Raman peak) at 520.6 cm^{-1}.

3. Results and discussion

As shown schematically in Fig. 1, the as-deposited samples have a 500 nm thick amorphous carbon layer with a sp^3 fraction around 50% on c-sapphire (Fig. 1(a)). After laser annealing with 0.6 Jcm^{-2}, the carbon layer converts into RGO/α-carbon/Q-carbon/Sapphire heterostructure with a thin layer of reduced graphene oxide (RGO) (Fig. 1(b)). Fig. 1(c) shows a qualitative plot of Gibbs free energy as a function of temperature for graphite, α-carbon, diamond, Q-carbon, and molten carbon, where molten carbon line due to higher slope (entropy) intersects free energy lines of different solid phases. At the intersections, different phases of graphene (G) or RGO, α-carbon, diamond, and Q-carbon are formed from molten carbon with increasing degree of undercooling [13]. The undercooling is the difference in equilibrium melting point and intersecting temperatures. Thus, G/RGO, α-carbon, diamond, and Q-carbon are formed at T_m, T_α, T_d, and T_Q, respectively. The high-resolution cross-section TEM results in Fig. 1(d) shows an amorphous structure for Q-carbon with some embedded diamond nanocrystallites with dimensions of 2–5 nm. The inset electron diffraction pattern shows diffused rings from Q-carbon corresponding random diamond tetrahedra, where two sharp diffraction spots from underlying sapphire substrate are also shown. The characteristic EELS spectrum from the Q-carbon is shown in Fig. 1(e), which has a sloping edge at 285 eV with a broad peak at 292 eV. From the Voigt profile fit of the EELS spectrum, the sp^3 was estimated to be about 80% and 20% sp^2; this is consistent with Raman results. The peak position for π* and σ* edges are shown at 285 eV and 292 eV, respectively.

A set of three samples having 400 nm α-carbon and 100 nm Q-carbon layers on sapphire after pulsed laser annealing were irradiated with 5 MeV Au^+ ions to a dose of 2.9×10^{15} ions cm^{-2} (sample #1), 5.9×10^{15} ions cm^{-2} (sample #2), and 8.8×10^{15} ions cm^{-2} (sample #3). These doses correspond to average damage doses of 3.3 dpa, 6.6 dpa, and 10 dpa (displacements per atom) in the Q-carbon layer, for samples 1, 2 and 3, respectively. Half of these samples were masked by thick metal foils to study the details of microstructural changes before and after ion irradiations. The results on depth distributions of damage and implanted Au concentration at the highest

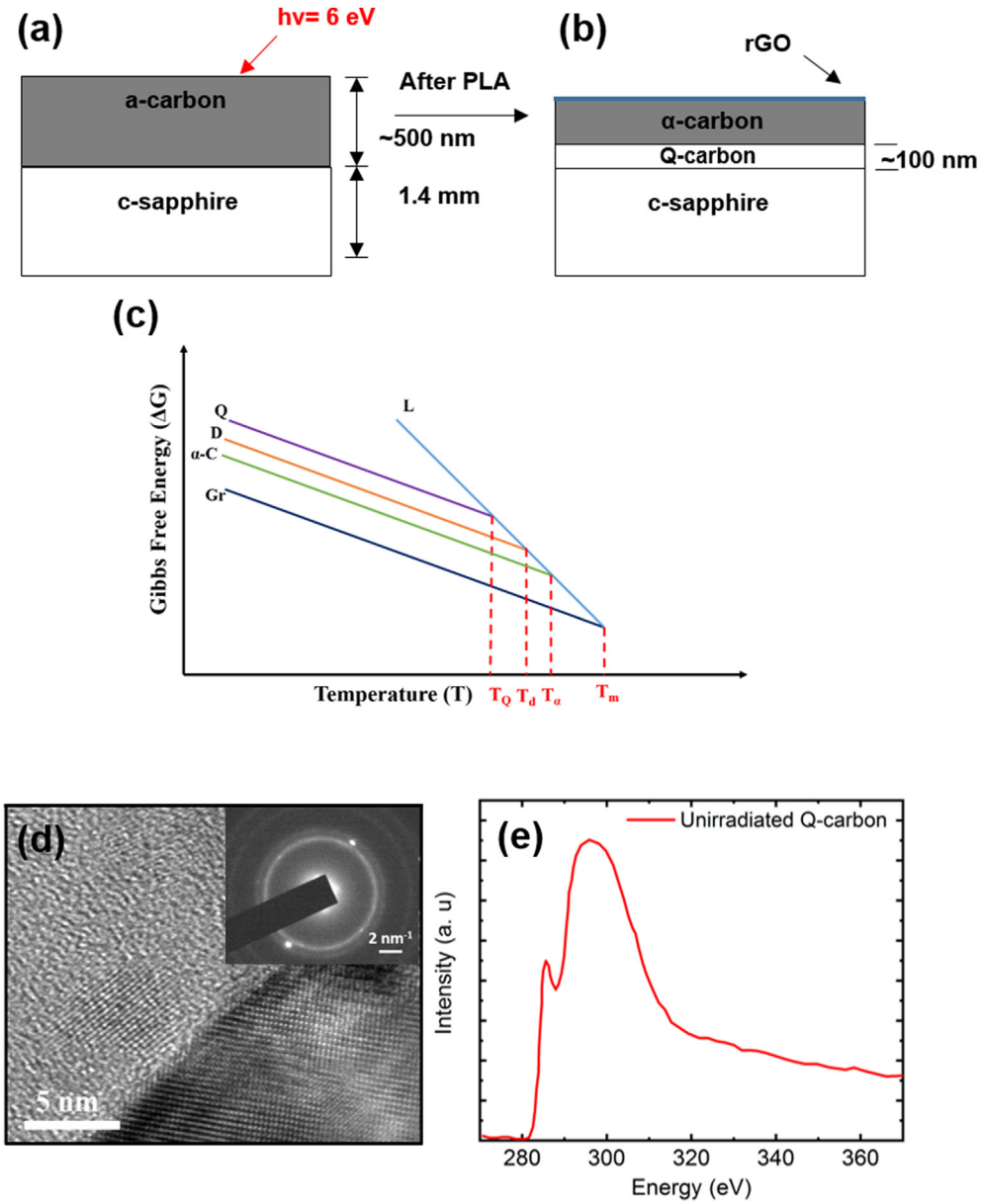

Fig. 1. (a) Schematic of samples before laser Irradiation, (b) after laser irradiation, (c) Gibbs free energy for different phases, (d) HRTEM cross-section showing the structure of Q-carbon with embedded 2 nm diamond, and (e) corresponding EELS from Q-carbon. (A colour version of this figure can be viewed online.)

fluence (8.8×10^{15} ions cm^{-2}) for 5 MeV Au^{+} ions using full-cascade TRIM calculations are shown in Fig. 2(a). The damage in terms of displacements per atom (dpa) as a function of depth is about 10 dpa in Q-carbon layer with damage peak of 40 dpa centered at 700 nm in the sapphire substrate. It is interesting to note that the sapphire, even after 40 dpa, shows no indication of amorphization (Fig. 2(a)). This figure also shows the implanted concentration of Au as a function of depth, where there is very little Au in α-carbon and Q-carbon layers, but it rises rapidly beyond 600 nm with a peak around 780 nm. Based on the simulation of 100,000 ions, the Au concentration is 1.5 appm at 470 nm for an ion fluence of 8.8×10^{15} ions/cm^2, and zero at shallower depths (i.e., the predicted Au concentration is close to zero appm at 460 nm and below). With the improved statistics, the Au concentration increases more smoothly with depth. The Au concentration on either side of the interface is much less than the C, Al, and O mixing concentrations. The peak concentration is 3800 appm, which corresponds to 0.38 at%. This is a mixed layer with high concentration of defects, but it does not show any sign of precipitation. Due to energy straggling, there is a distribution (not wide) of ion energies and stopping powers in the Q-carbon layer. Based on the SRIM calculations, the average stopping powers (Energy Loss) in the Q-Carbon layer are: electronic stopping power = 7.12 keV/nm, and nuclear stopping power = 5.55 keV/nm, as shown in Fig. 2(b). This value of nuclear stopping translates into over 1840 eV per atom in Q-carbon. The Q-carbon can tolerate this amount of nuclear stopping, in addition to electronic excitations of 7.12 keV/nm, without any changes in structure and bonding characteristics, as discussed below. It should be noted that this value is considerably higher than 16eV per atom at which crystalline diamond accumulates enough defects to undergo first-order crystalline to amorphous phase transformation [8]. This study shows that the Q-carbon is able to withstand a total stopping power of more than 12.7 keV/nm, which is extremely high from radiation hardness considerations.

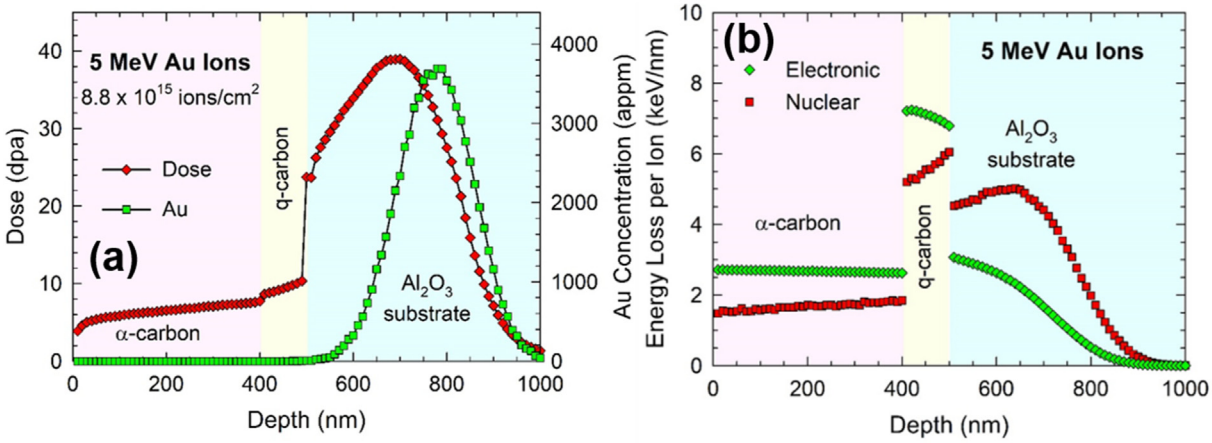

Fig. 2. (a) Depth distribution of damage and implanted Au concentration for 5 MeV Au^+ ions using full-cascade TRIM calculations; and (b) nuclear and electronic stopping powers as a function of depth. (A colour version of this figure can be viewed online.)

Fig. 3 (a) and (b) show SEM micrographs from masked (unirradiated) and ion irradiated regions of 3.3-dpa sample, respectively. The unirradiated region shows a thin RGO on the surface, whereas irradiated region shows only α-carbon, indicating that RGO has been sputtered off by energetic ions. The inset in Fig. 3(b) shows an onset of peeling off of α-carbon layer. The Raman spectrum (Fig. 3(c)) from unirradiated sample shows characteristic RGO bonding with higher G compared to D peak. The Raman spectrum in Fig. 3(d) contains characteristic α-carbon structure with 60% sp^3 bonding. This is consistent with SEM data, showing sputtering of RGO. The Q-carbon layer spectrum is not visible due to a large (~400 nm) thickness of α-carbon overlayer.

After 6.6 dpa, the α-carbon layer has peeled off, and the boundary between unirradiated (left) and irradiated (right) regions is shown in Fig. 4(a). At a higher magnification (Fig. 4(b)), the boundary clearly shows RGO and α-carbon layer in the unirradiated (left) and irradiated Q-carbon layer (right). At a still higher magnification, Fig. 4(c) shows Q-carbon and the presence nanodiamonds with average size 60 nm. These nanodiamonds have grown from an average size of 2 nm to 60 nm after ion irradiation of 6.6 dpa. The presence of diamond phase was confirmed by the characteristic EBSD pattern, shown in the inset of Fig. 4(c). This growth of metastable diamond nuclei after ion irradiation is really exciting, and it will be discussed below. The Raman spectrum from the 6.6 dpa sample shows that Q-carbon structure has not changed after irradiation (Fig. 4(d)). This will be confirmed by high-

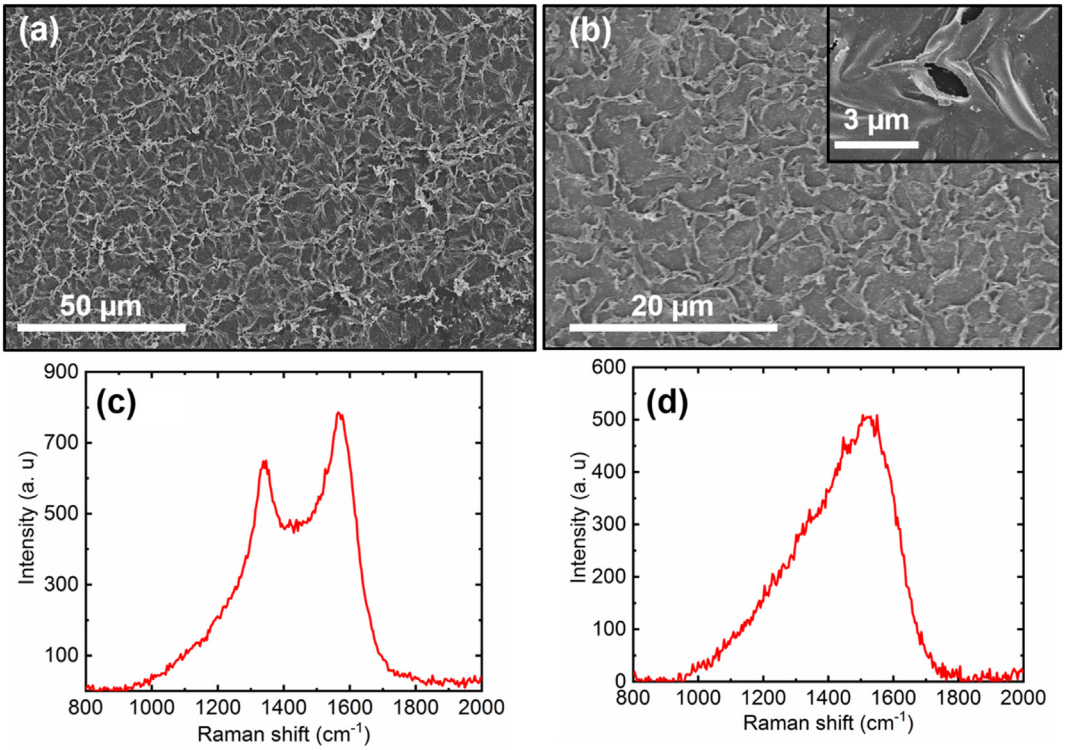

Fig. 3. (a) HRSEM micrograph before ion irradiation; (b) after ion irradiation of sample #1; (c) Raman spectrum from unirradiated region; and (d) Raman spectrum from irradiated region. (A colour version of this figure can be viewed online.)

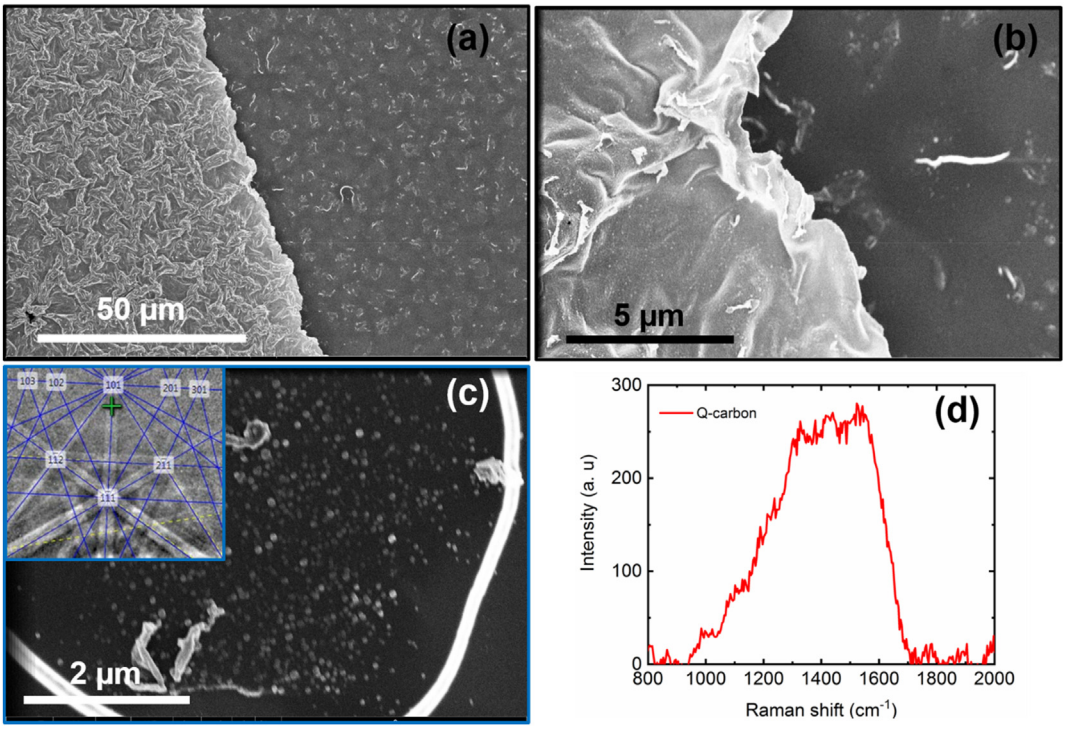

Fig. 4. HRSEM micrographs from sample #2 with unirradiated and irradiated regions with increasing magnification (a&b); (c) growth of nanodiamonds with ion irradiation with inset showing characteristic diamond EBSD pattern; and (d) Raman spectrum from irradiated region with nanodiamond peak at 1328 cm^{-1}. (A colour version of this figure can be viewed online.)

resolution EELS studies below. It is interesting to note that there is a nanodiamond peak at 1328 cm^{-1} embedded in the Raman Q-carbon spectrum, which is in agreement with HRSEM results.

The HRSEM results after the 10 dpa ion irradiation showed the Q-carbon layer with embedded nanodiamonds. It is very interesting that the nanodiamonds have shrunk from 60 nm in the 6.6 dpa sample to 40 nm in 10 dpa sample, as shown in Fig. 5(a). The inset EBSD in Fig. 5(a) confirms the diamond structure of

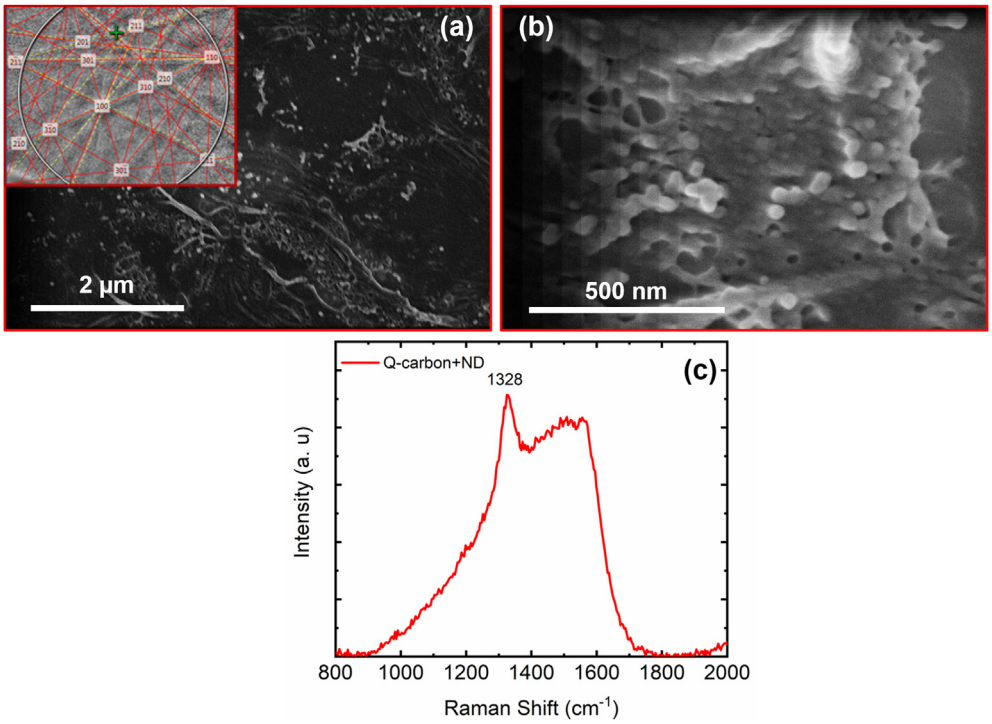

Fig. 5. a) HRSEM micrograph from sample #3 from irradiated region, showing Q-carbon and shrinkage of nanodiamonds (identified by inset diamond EBSD); (b) detailed size distribution at a higher magnification; and (c) Raman spectrum from irradiated region with nanodiamond peak at 1328 cm^{-1}. (A colour version of this figure can be viewed online.)

nanodiamonds. At a higher magnification (Fig. 5(b)), the faceted nanodiamonds are clearly seen. However, there are areas, where nanodiamonds seem to have dissolved completely. The Raman spectrum from this sample is shown in Fig. 5(c), showing a characteristic Q-carbon with embedded nanodiamond peak at 1328 cm^{-1}. This downshift is attributed to phonon confinement effects in nanodiamonds.

Fig. 6(a) shows cross-section HAADF image of unirradiated sample just after the laser annealing treatment, where 100 nm thick layer Q-carbon has formed. At a higher magnification (Fig. 6(b)), HAADF imaging along the [120] axis shows the interface between Q-carbon and sapphire exhibits an about 1 nm mixed Al_4C_3 amorphous layer. The formation of this layer occurs as a result of reaction between molten carbon and aluminum oxide has been discussed in detail in an earlier paper [13]. The Al_2O_3 has trigonal structure with space group R_{3c} and lattice constant (a = 0.478 nm, c = 1.299 nm), which are widely different from those of Al_4C_3 (rhombohedral, space group *R*3*m*, lattice constant: a = 0.3335 nm, b = 0.3335 nm, c = 0.85422 nm, $\alpha = 78.743^\circ$, $\beta = 78.743^\circ$, $\gamma = 60^\circ$). As a result, Al_4C_3 is not able to grow epitaxially on Al_2O_3 and turns amorphous upon quenching. The EELS of Q-carbon before ion irradiation is shown in Fig. 6(c) with characteristic π*peak at 285eV and broad σ*peak at 292eV. The EELS of aluminum oxide before irradiation shows characteristic Al-L sharp peak at 79.5 eV and a broad peak at 98.5eV (Fig. 6(d)).

Fig. 7 shows a summary HAADF and EELS results after irradiation to 3.3 dpa (sample #1). The HAADF cross-section image (Fig. 7(a) shows Q-carbon, and ion beam mixed (IBM) layer (4 nm thick) below the Q-carbon layer. The EELS results from Q-carbon (Fig. 7(b)) shows that the spectrum has remained unchanged with characteristic π*peak at 285eV and broad σ*peak at 292eV, showing that bonding characteristics have not been affected by ion irradiation. The EELS from the IBM layer (Fig. 7(c)) shows the peaks centered on 79.5 eV and 99.0 eV for Al_2O_3, and a shoulder at 77.5eV corresponding to Al_4C_3. This is consistent with a mixture of amorphous Al_4C_3 (with a peak at (77.5 eV)) and Al_2O_3 (peak at 79.5 eV). The EELS spectrum from irradiated Al_2O_3 with characteristic Al-L sharp peak at 79.5 eV and a broad peak at 98.5 eV, as shown in Fig. 7(d) has remained unaffected, signifying that the bonding characteristics in alumina also have not been affected by the ion irradiation.

The HAADF and EELS results after irradiation with 10 dpa (sample #3) are summarized in Fig. 8. The HAADF cross-section image (Fig. 8(a) shows Q-carbon, and ion beam mixed (IBM) layer below the Q-carbon layer. It is interesting to note that IBM layer after 10 dpa has increased to 10 nm. The EELS results from Q-carbon (Fig. 8(b)) show that the spectrum has remained unchanged with characteristic π*peak at 285 eV and broad σ*peak at 292 eV,

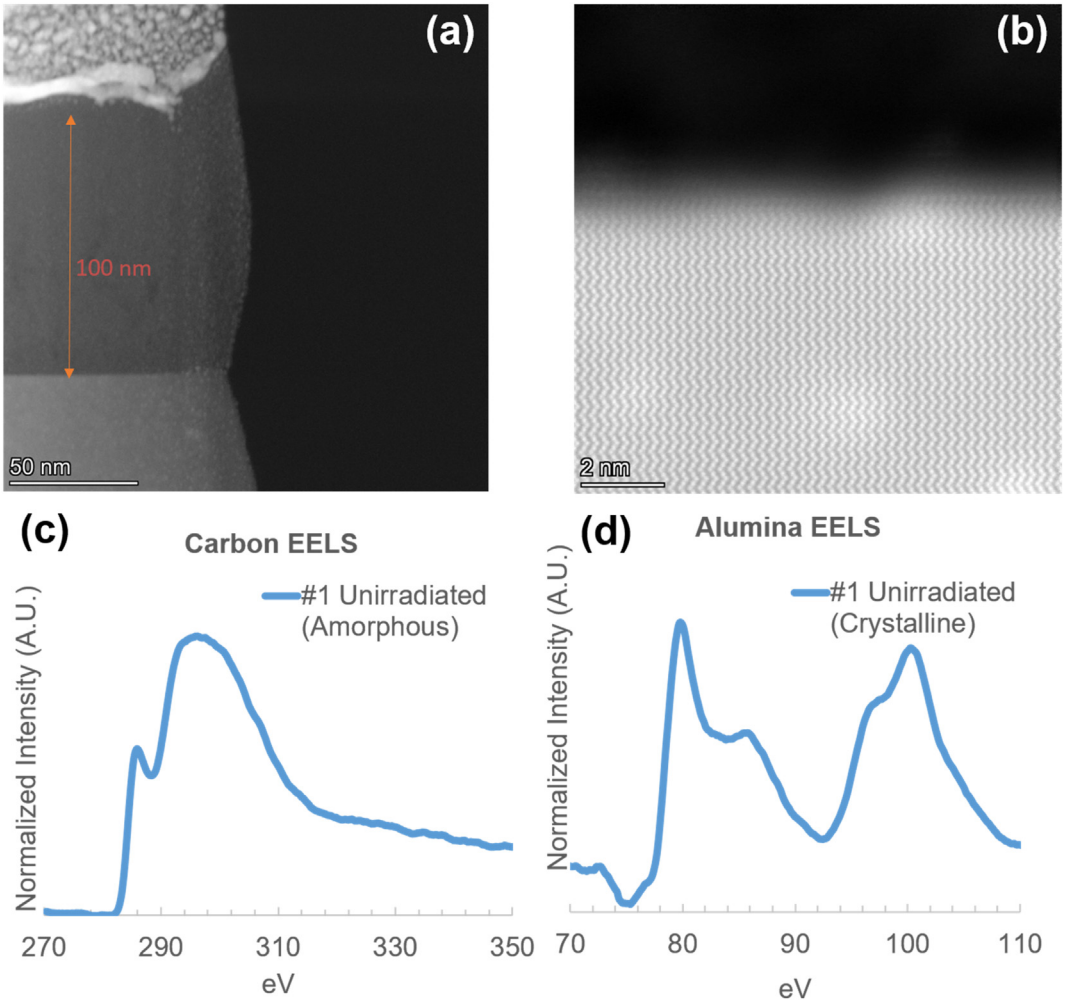

Fig. 6. (a) HAADF cross-section showing 100 nm Q-carbon on sapphire; (b) high-resolution HAADF image of unirradiated sample with Q-carbon and about 1 nm mixed Al_4C_3 amorphous layer; (c) EELS of Qcarbon before ion irradiation with characteristic π*peak at 285eV and broad σ*peak at 292eV; and (d) EELS of aluminum oxide with characteristic Al-L sharp peak at 79.5 eV and a broad peak at 98.5eV. (A colour version of this figure can be viewed online.)

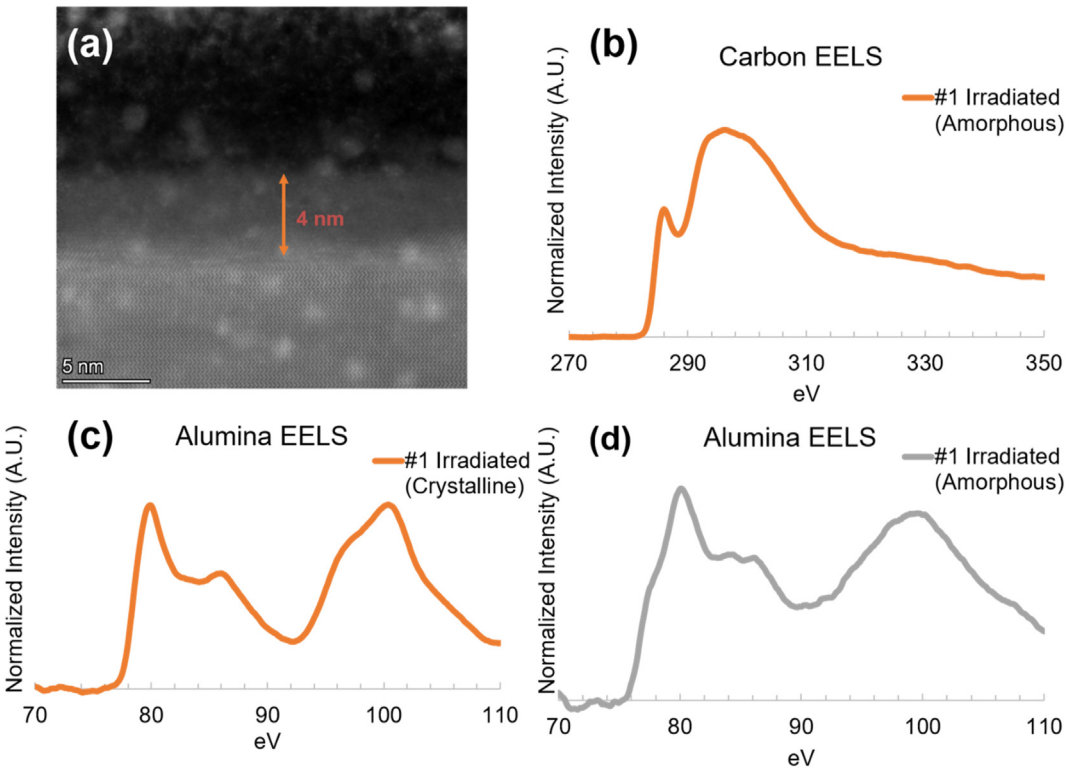

Fig. 7. (a) HAADF cross-section image from sample #1 with Q-carbon and ion beam mixed (IBM) layer (5 nm thick) below the Q-carbon layer; (b) EELS results from Q-carbon with characteristic π*peak at 285eV and broad σ*peak at 292eV; (c) EELS from the IBM layer with broad peaks centered on 79.5eV and 99.0eV; and (d) EELS spectrum from irradiated Al_2O_3 with characteristic Al-L sharp peak at 79.5 eV and a broad peak at 98.5eV. (A colour version of this figure can be viewed online.)

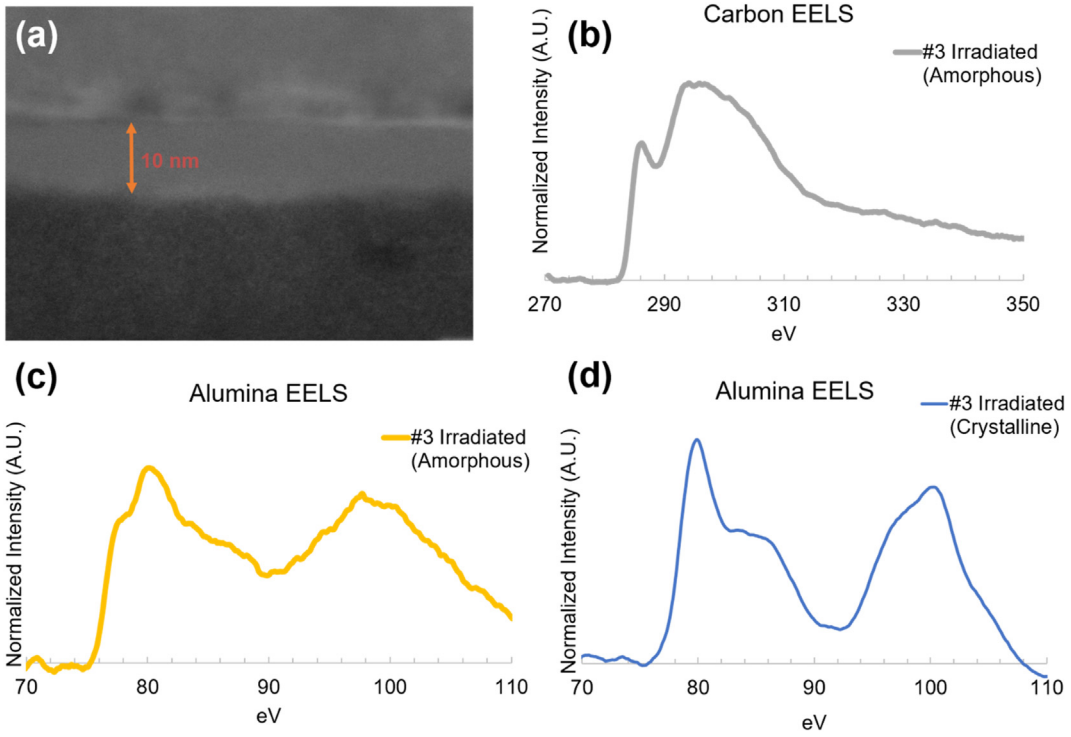

Fig. 8. (a) HAADF cross-section image from sample #3 with Q-carbon and ion beam mixed (IBM) layer (5 nm thick) below the Q-carbon layer; (b) EELS results from Q-carbon with characteristic π*peak at 285eV and broad σ*peak at 292eV; (c) EELS from the IBM layer (10 nm thick) with broad peaks centered on 79.5eV and 99.0eV; and (d) EELS spectrum from irradiated Al_2O_3 with characteristic Al-L sharp peak at 79.5 eV and a broad peak at 98.5eV. (A colour version of this figure can be viewed online.)

showing that bonding characteristics have not been affected by 10 dpa of ion irradiation. The EELS from the IBM layer (Fig. 8(c)) shows the peaks centered on 79.5 eV and 99.0 eV for Al_2O_3, and a shoulder at 77.5 eV corresponding to Al_4C_3. This is consistent with a mixture of amorphous Al_4C_3 (with a peak at (77.5 eV)) and Al_2O_3 (peak at 79.5 eV). The EELS spectrum from irradiated Al_2O_3 with characteristic Al-L sharp peak at 79.5 eV and a broad peak at 98.5 eV, as shown in Fig. 8(d), has remained unaffected, signifying that the bonding characteristics in alumina have not been affected by the ion irradiation.

In designing radiation resistant materials, we need to consider two critical factors: (1) minimize damage production; and (2) enhance damage repair mechanisms. Since the Q-carbon consists of diamond carbon tetraheda, which are randomly packed with over 80% packing efficiency. There is sp^3 bonding within the tetrahedra, and sp^2bonding between the tetrahedra. This makes Q-carbon to be covalently bonded and the strongest material with hardness exceeding that of diamond by 60% [9]. These factors and the high atomic packing minimize damage production by increasing the damage threshold energy beyond that for diamond, which was assumed in the SRIM calculations. The repair mechanism is derived from its amorphous structure and the presence of dangling bonds. Thus displaced atoms repair other dangling bonds, leaving the material damage neutral. The presence of dangling bonds with unpaired spins was shown to create a robust ferromagnetism at room temperature in Q-carbon [10].

3.1. Ion beam mixing

Previous results on ion beam irradiation in alumina have shown that ion beam mixing in alumina is limited to ballistic mixing of less than 5 nm and only to those layers which form thermodynamically stable phases [18,19]. Our results show an increase in IBM layer thickness with ion dose. Since the temperature rise during irradiation was estimated to be less than 10K, the diffusivity of carbon (during irradiation is very limited, we propose that ballistic mixing continues to occur with increasing dose during ion irradiation.

Ballistic Ion beam mixing occurs as a result of enhanced forward scattering, which kicks carbon atoms ballistically from the Q-carbon layer into the alumina substrate. These energetic carbon atoms break Al-O bonds and form Al_4C_3 - Al_2O_3 amorphous phase. From the damage profile (as shown in Fig. 2), alumina does not amorphize even at 40 dpa peak, which occurs at 700 nm and is 200 nm below the Q-carbon layer. Fig. 9 (a) shows the carbon recoil spectrum (from SRIM calculations) within 20 nm of the Q-carbon and alumina interface, where most of the recoils are less than 5 keV are responsible for the formation of the IBM layer. The SRIM calculated concentration of C, Al, and O profiles at a fluence 8.8×10^{15} ions cm^{-2} (in Fig. 9 (b)) show that enhanced forward scattering results in a significant C concentration in alumina, and very little Al and O in the Q-carbon layer. The carbon concentration is quite significant (25 at%) into sapphire near the interface, particularly within 10 nm of the interface (Fig. 2(b)). This concentration is consistent with 50%Al_2O_3+50% Al_4C_3. The thickness of ion-beam mixed layer was found to increase from 5 nm at 3.3 dpa to 10 nm at 10 dpa. While the overall sample temperature is not significantly increased, the formation of the amorphous Al_4C_3 phase may be driven by the highly localized thermal spike (about 10–100 ps duration) associated with each ion with a total energy deposition of 12.7 keV/nm (about 16 eV/atom over a diameter of 2 nm) per ion at the interface.

3.2. Growth and shrinkage of nanodiamonds by ion irradiation

The growth of equilibrium phases such as Ag precipitates in amorphous silicate glass under ion irradiations has been addressed in previous studies [20]. Here we address the growth of nonequilibrium metastable phase of diamond in amorphous Q-carbon as a result of ion irradiation. The growth of nanodiamonds from 3.3 nm before irradiation to 60 nm after 6.6 dpa of ion irradiation (as shown in Fig. 4 (c)) is extremely interesting. This shows that ion beam irradiation can be used to grow nanodiamonds in a controlled way for applications ranging from quantum computing and quantum communication to nanosensing. Since diamond is a nonequilibrium metastable phase, its growth requires nonequlibrium aspects involving energetic particles far beyond kT. We have shown that diamond can be grown epitaxially on diamond and c-BN under pulsed laser deposition with energetic carbon species (average energy 16 eV) [21]. In view of these results, we propose that energetic carbon recoils around nanodiamonds can overcome the growth activation free energy and attach to diamond/Q-carbon interface. The shrinkage is explained if the free energy curve reverses as we pump in more defects in diamond and Q-carbon. At this point, the atoms jumping from the diamond to Q-carbon can lower the free energy and we observe shrinkage instead of growth, as shown in Fig. 5 (a,b).

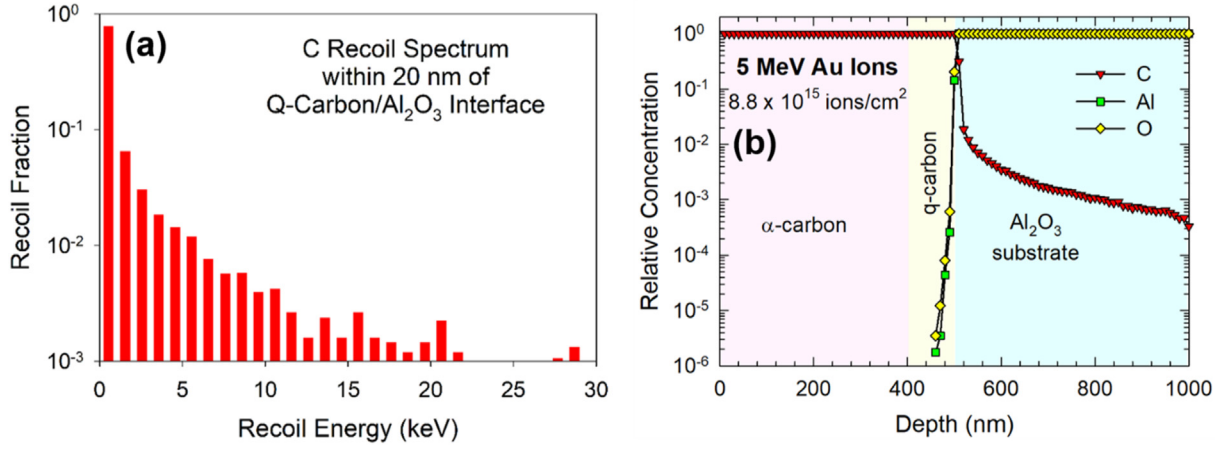

Fig. 9. (a) Carbon recoil spectrum within 20 nm of Q-carbon and alumina interface; and (b) concentration of C, Al, and O profiles with significant C concentration in alumina, and very little Al and O in Q-carbon layer. (A colour version of this figure can be viewed online.)

4. Summary and conclusions

In summary, we have shown that Q-carbon is extremely resistant to heavy ion radiation damage, involving extreme atomic displacements and electronic excitations. Using 5 MeV Au $^{+}$ ions, the Q-carbon films on sapphire substrates were irradiated to doses, ranging from 2.9×10^{15} ions cm^{-2} to C ions cm^{-2}, corresponding to the range of 3.3–10 dpa. After ion irradiations, detailed studies on atomic structure were carried out using high-resolution transmission electron microscopy (HRTEM and HAADF), and bonding characteristics were studied by using electron-energy-loss spectroscopy (EELS) and Raman spectroscopy. These studies on samples before and after ion irradiations show that atomic structure and bonding characteristics of Q-carbon as well as sapphire substrate have remained essentially unchanged after 10 dpa of radiation damage, which is equivalent to over twenty years of neutron damage in a conventional reactor. Future applications may include moderator for fission reactors and inner wall coatings for fusion reactors, in addition to coating of solid state electronics. Coating of Q-carbon on sapphire screens will prevent damage to wide range of cell phones and satellite communication devices.

CRediT authorship contribution statement

J. Narayan: Developing the concept and interpreting the data. **P. Joshi:** Performing SEM and Raman studies. **J. Smith:** Performing HRTEM and EELS. **W. Gao:** Supervising HRTEM and EELS. **W.J. Weber:** Ion irradiations and simulations. **R.J. Narayan:** Supervising SEM and Raman studies.

Declaration of competing interest

The authors declare that they have no known competing financial interests or personal relationships that could have appeared to influence the work reported in this paper.

Acknowledgments

This work was supported by the National Science Foundation (NSF DMR-2016256).

References

[1] Y. Guérin, G.S. Was, S.J. Zinkle, Materials challenges for advanced nuclear energy systems, MRS Bull. 34 (2009) 10–19, https://doi.org/10.1017/S0883769400100028.
[2] Y. Zhang, W.J. Weber, Ion irradiation and modification: the role of coupled electronic and nuclear energy dissipation and subsequent nonequilibrium processes in materials, Appl. Phys. Rev. 7 (2020), 041307, https://doi.org/10.1063/5.0027462.
[3] J. Narayan, O.W. Holland, Characteristics of ion-implantation damage and annealing phenomena in semiconductors, J. Electrochem. Soc. 131 (1984) 2651–2662, https://doi.org/10.1149/1.2115377/PDF.
[4] A.J. McKenna, T. Trevethan, C.D. Latham, P.J. Young, M.I. Heggie, Threshold displacement energy and damage function in graphite from molecular dynamics, Carbon 99 (2016) 71–78, https://doi.org/10.1016/J.CARBON.2015.11.040.
[5] J. Koike, D.M. Parkin, T.E. Mitchell, Displacement threshold energy for type IIa diamond, Appl. Phys. Lett. 60 (1992) 1450, https://doi.org/10.1063/1.107267.
[6] J. Narayan, D. Fathy, O.S. Oen, O.W. Holland, Atomic structure of ion implantation damage and process of amorphization in semiconductors, J. Vac. Sci. Technol. A Vac. Surf. Film. 2 (1984) 1303–1308, https://doi.org/10.1116/1.572399.
[7] Y. Zhang, T. Egami, W.J. Weber, Dissipation of radiation energy in concentrated solid-solution alloys: unique defect properties and microstructural evolution, MRS Bull. 44 (2019) 798–811, https://doi.org/10.1557/MRS.2019.233.
[8] S. Prawer, R. Kalish, Ion-beam-induced transformation of diamond, Phys. Rev. B 51 (1995) 15711–15722, https://doi.org/10.1103/PHYSREVB.51.15711.
[9] J. Narayan, A. Bhaumik, Novel phase of carbon, ferromagnetism, and conversion into diamond, J. Appl. Phys. 118 (2015), 215303, https://doi.org/10.1063/1.4936595.
[10] A. Bhaumik, R. Sachan, S. Gupta, J. Narayan, Discovery of high-temperature superconductivity (Tc = 55 K) in B-doped Q-carbon, ACS Nano 11 (2017) 11915–11922, https://doi.org/10.1021/ACSNANO.7B06888.
[11] J. Narayan, S. Gupta, A. Bhaumik, R. Sachan, F. Cellini, E. Riedo, Q-carbon harder than diamond, MRS Commun 8 (2018) 428–436, https://doi.org/10.1557/mrc.2018.35.
[12] J. Narayan, A. Bhaumik, S. Gupta, A. Haque, R. Sachan, Progress in Q-carbon and related materials with extraordinary properties, 6, 2018, pp. 353–364, https://doi.org/10.1080/21663831.2018.1458753.
[13] J. Narayan, A. Bhaumik, S. Gupta, P. Joshi, P. Riley, R.J. Narayan, Role of Q-carbon in nucleation and formation of continuous diamond film, Carbon 176 (2021) 558–568, https://doi.org/10.1016/j.carbon.2021.02.049.
[14] R. Sachan, S. Gupta, J. Narayan, Nonequilibrium structural evolution of Q-carbon and interfaces, ACS Appl. Mater. Interfaces 12 (2019) 1330–1338, https://doi.org/10.1021/ACSAMI.9B17428.
[15] Y. Zhang, M.L. Crespillo, H. Xue, K. Jin, C.H. Chen, C.L. Fontana, J.T. Graham, W.J. Weber, New ion beam materials laboratory for materials modification and irradiation effects research, Nucl. Instrum. Methods Phys. Res. Sect. B Beam Interact. Mater. Atoms 338 (2014) 19–30, https://doi.org/10.1016/J.NIMB.2014.07.028.
[16] J.F. Ziegler, M.D. Ziegler, J.P. Biersack, SRIM – the stopping and range of ions in matter, Nucl. Instrum. Methods Phys. Res. Sect. B Beam Interact. Mater. Atoms 268 (2010) 1818–1823, https://doi.org/10.1016/J.NIMB.2010.02.091, 2010.
[17] W.J. Weber, Y. Zhang, Predicting damage production in monoatomic and multi-elemental targets using stopping and range of ions in matter code: challenges and recommendations, Curr. Opin. Solid State Mater. Sci. 23 (2019), 100757, https://doi.org/10.1016/J.COSSMS.2019.06.001.
[18] E.A. Cooper, M. Nastasi, Ion beam mixing of marker layers into amorphous aluminum oxide, Nucl. Instrum. Methods Phys. Res. Sect. B Beam Interact. Mater. Atoms 91 (1994) 558–561, https://doi.org/10.1016/0168-583X(94)96285-5.
[19] C.J. McHargue, D.L. Joslin, C.W. White, Ion beam mixing in insulator substrates, Nucl. Instrum. Methods Phys. Res. Sect. B Beam Interact. Mater. Atoms 91 (1994) 549–557, https://doi.org/10.1016/0168-583X(94)96284-7.
[20] J.C. Pivin, G. Roger, M.A. Garcia, F. Singh, D.K. Avasthi, Nucleation and growth of Ag clusters in silicate glasses under ion irradiation, Nucl. Instrum. Methods Phys. Res. Sect. B Beam Interact. Mater. Atoms 215 (2004) 373–384, https://doi.org/10.1016/J.NIMB.2003.07.002.
[21] J. Narayan, A. Bhaumik, W. Xu, Direct conversion of h-BN into c-BN and formation of epitaxial c-BN/diamond heterostructures, J. App. Phys. 119 (2016), https://doi.org/10.1063/1.4948688.